

Article

Brightness Temperature Characteristics of Short-Duration Heavy Rainfall in the Chengdu–Chongqing Railway Region in China

Xinchao Liu ^{1,2}, Yongren Chen ^{2,3,4,*} , Jie Guo ^{1,2}, Wenwen Song ^{1,2} and Jia Dan ^{1,2}

¹ Sichuan Meteorological Service Centre, Sichuan Provincial Meteorological Service, Chengdu 610072, China; liuxc82@163.com (X.L.); guojie126@163.com (J.G.); songww8682@sina.com (W.S.); soldan@163.com (J.D.)

² Heavy Rain and Drought–Flood Disasters in Plateau and Basin Key Laboratory of Sichuan Province, Chengdu 610072, China

³ Meteorological Disaster Defense Technology Center, Sichuan Provincial Meteorological Service, Chengdu 610072, China

⁴ Institute of Plateau Meteorology, China Meteorological Administration, Chengdu 610072, China

* Correspondence: yr20060004@163.com

Abstract: In this study, we analyzed the brightness temperature characteristics of short-duration heavy rainfall (SDHR) along the Chengdu–Chongqing Railway (CCR), an important corridor of economic and transportation activity in southwest China. Our findings could prove useful in the monitoring and advance warning of SDHR events: (1) SDHR predominantly occurred from July to August, with a peak frequency in July in the CCR area. In terms of diurnal variation, SDHR was mainly observed at night, particularly between 22:00–05:00 and 06:00–09:00 (local time), with a peak at 01:00; (2) The relationship between SDHR and equivalent blackbody temperature (TBB) further showed that the occurrence of SDHR was accompanied by TBB decreasing to its minimum value, after which it increased, and SDHR ceased. In cases where TBB approached its minimum value after 1 h but continued to decrease slightly, SDHR continued. When SDHR occurred, the majority of the TBB values were recorded in the range 190–230 K; within this range, values between 190 and 200 K were most frequently recorded. In general, lower TBB values are associated with more intense SDHR. Based on this finding, we used linear regression to establish an estimating equation for SDHR.

Keywords: short-duration heavy rainfall (SDHR); FY-4A; Chengdu–Chongqing Railway; TBB



Citation: Liu, X.; Chen, Y.; Guo, J.; Song, W.; Dan, J. Brightness Temperature Characteristics of Short-Duration Heavy Rainfall in the Chengdu–Chongqing Railway Region in China. *Atmosphere* **2023**, *14*, 896. <https://doi.org/10.3390/atmos14050896>

Academic Editor: Tomeu Rigo

Received: 11 April 2023

Revised: 17 May 2023

Accepted: 19 May 2023

Published: 20 May 2023



Copyright: © 2023 by the authors. Licensee MDPI, Basel, Switzerland. This article is an open access article distributed under the terms and conditions of the Creative Commons Attribution (CC BY) license (<https://creativecommons.org/licenses/by/4.0/>).

1. Introduction

Short-duration heavy rainfall (SDHR) is one of the most common severe convective weather types in China. SDHR events have a short duration and high intensity, occur suddenly, are difficult to predict, and can have disastrous consequences. They frequently trigger natural disasters such as flash floods in mountainous regions, debris flows, and landslides [1,2], and can significantly impact railway activity [3–5]. With the increasing trend towards extreme precipitation events, the disasters caused by SDHR are likely to become an even more significant issue [6–12].

In light of this, meteorologists have carried out a considerable amount of research work on SDHR. Several studies have revealed the temporal and spatial distribution characteristics of SDHR [13–16]. Chen et al. [1] examined the frequency of occurrence of SDHR events and heavy rainfall (daily rainfall > 50 mm) over mainland China and showed that their spatial distributions were similar. SDHR events occur most frequently in July, followed by August. There are records of extreme precipitation as early as April in southern China, while extreme rainfall does not occur in northern China until late June [17]. A study by Zhang and Zhai [18] showed that extreme precipitation events occurred most frequently in the late afternoon and/or early evening over Yunnan, South China, North China, and Northeast China. In the Guizhou Plateau and the Sichuan Basin, extreme

precipitation events occurred most frequently late at night and/or early in the morning. In the western Sichuan Plateau, such events occurred most frequently in the middle of the night. Zheng et al. [19] demonstrated that extreme precipitation patterns were bimodal over the whole of central and eastern China, with a primary peak occurring in the late afternoon and a secondary peak between midnight and the early morning.

A number of meteorologists have studied aspects of the synoptic background of SDHR events, including extreme hourly precipitation [16,20,21], and SDHR has been shown to be related to urban change [15,16,22–24]. In some mega cities, in particular, SDHR showed a distinct urban rain-island feature as a result of urbanization [23]; the correlation between the intensity of the urban heat island effect and the frequency of SDHR was also found to be highly significant for a period of more than 3 h before SDHR events [25]. In the Pearl River Delta, China, the pronounced urban heat island effect has also been found to also enhance extreme hourly precipitation, especially over the inland urban region, where the urban heat island intensity is strongest [26].

The effects of the physical environment, satellite and radar data, and other aspects of SDHR have also received research attention. Tian et al. [27] asserted that total precipitable water was the best parameter by which to measure hourly rainfall intensity. Li et al. [25] showed that the occurrence of SDHR events coincided with the distribution of surface warming and increased humidity as well as organized convergence in the presence of an unstable environment. Meng et al. [28] reported that mesoscale convective systems (MCSs) were responsible for about 60% of SDHR events. Ma et al. [29] found that SDHR is most likely to occur when bow echoes are observed. In a study by Zou et al. [30], approximately 43% of SDHR events were shown to be accompanied by lightning activity (SDRWL events). The rainfall intensity of SDRWL events was significantly higher than that of SDHR events during which lightning did not occur. These studies have played an important role in understanding SDHR in China.

Heavy precipitation occurs frequently over southwest China. SDHR events are primarily caused by MCSs; on satellite cloud maps, the brightness temperature of the clouds over these areas of heavy precipitation has been found to be low [31–36].

As an important railway in southwest China, the Chengdu–Chongqing Railway (CCR), which runs from Chengdu in the west Sichuan Basin to Chongqing in the east Sichuan Basin, serves as an economic and transportation artery, connecting the Chengdu–Chongqing economic circle. The CCR is located in the Sichuan Basin on the east side of the Tibetan Plateau (Figure 1). Due to the effects of its unique topography and airflow, the intensity of extreme precipitation events over the Sichuan Basin is significantly higher than that over the Sichuan Plateau [37]. The frequency of SDHR is also higher over the Sichuan Basin [38–40], meaning that SDHR events frequently affect the CCR. It is, therefore, necessary to study the SDHR to obtain valuable meteorological information and ensure the safe operation of the railway. SDHR events are difficult to forecast, and the forecast accuracy of SDHR along the CCR, in particular, is in urgent need of improvement. To achieve this, we will use satellite data to analyze SDHR, explore the relationship between equivalent black body temperature (TBB) and SDHR, and establish an estimating equation that could enable more accurate forecasting and provide an early warning of SDHR events.

The following section, Section 2, describes the data and methods used in this study; Section 3 describes the spatiotemporal distribution characteristics of SDHR; Section 4 analyses the relationship between SDHR and TBB and its estimating equation; and Section 5 provides a conclusion.

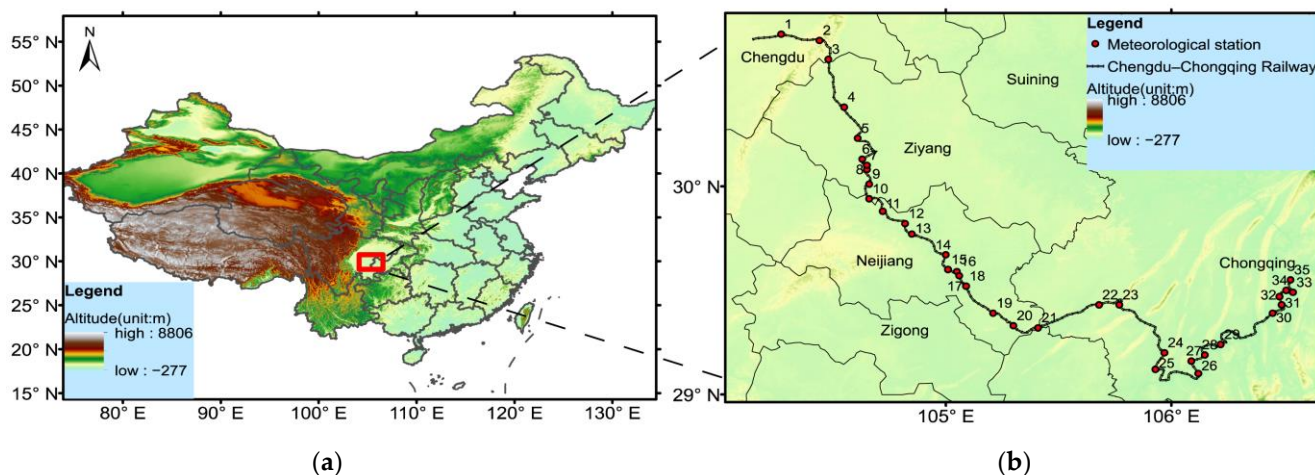


Figure 1. (a) The geographical location of the Chengdu–Chongqing Railway and (b) the distribution of meteorological stations along the railway. (Note: The numbers in (b) correspond to the following meteorological stations. 1: Shibantan, 2: Renhe, 3: Wufeng, 4: Jiangyang, 5: Shuijing, 6: Sanxian River, 7: Zixi, 8: Songtao, 9: Zhongyi, 10: Shuangfeng Temple, 11: Lugao Mountain, 12: Yangliu Beach, 13: Zizhong, 14: Fuxi, 15: Jingmin Sihe, 16: Teachers College, 17: City Station, 18: Xindu, 19: Yingxiang, 20: Longchang, 21: Sanhe Village, 22: Fenggao, 23: Dongsheng Village, 24: Longdong Bridge, 25: Ciba Station, 26: Hengshan, 27: Jingang Reservoir, 28: Youxi, 29: Yihai Kerry, 30: Shatuo Village, 31: Eggplant Stream, 32: Jiugong Temple, 33: Huangjueping, 34: Yangjiaping, 35: Fotuguan).

2. Data and Methods

Data from the Fengyun-4A (FY-4A) satellite and ground-based observational precipitation data were used in this study.

The FY-4A satellite is an example of China's new generation of geostationary meteorological satellites. It was successfully launched on 11 December 2016, completed in-orbit tests in early 2018, and was officially put into operation on 1 May 2018. FY-4A carries four new instruments: the advanced geosynchronous radiation imager (AGRI), the geosynchronous interferometric infrared sounder (GIIRS), the lightning mapping imager (LMI), and the Space Environment Package (SEP). It has 14 channels and can scan every 5 min with a subsatellite point resolution of 0.5–4 km; it can capture data at high spatial and temporal resolutions, with continuous observation capabilities and a wide range [41]. It provides a better data base for monitoring extreme weather such as heavy rainfall. Some meteorologists have used FY-4A satellite data to analyze heavy rainfall [42–44], but few studies on SDHR have been published. In our study, we used TBB data to analyze the brightness temperature characteristics of SDHR.

The TBB data from FY-4A (<http://www.nsmc.org.cn/nsmc/en/home/index.html> (accessed on 10 April 2023)) has a spatial resolution of 4 km. We used the 12 μm TBB data from channel 13 of FY-4A's AGRI. As the FY-4A satellite conducts a full-disk observation every hour, and the scanning time is 15 min, three consecutive full-disk observations were conducted every 3 h. For periods for which full-disk data were not available, 5-min observations of the China region were used here. Thus, the observational data for the full disk and the China region were complementary in this study.

Hourly precipitation data for 2019–2020 were obtained from meteorological stations in Sichuan and Chongqing. Hourly precipitation of 20 mm and above was defined as SDHR [1,15,18,19,27,28]. Thirty-five stations along the length of the CCR were selected, each of which was situated within 1 km of the railway (Figure 1). An SDHR event was judged to have occurred when an hourly rainfall value ≥ 20 mm was recorded at a given station, and the times and dates were logged for each such occurrence.

Pearson's correlation coefficient (PCC) was used to analyze the correlation between SDHR and TBB [45]; this approach was based on the assessment of linear correlation, as shown in Equation (1):

$$r = \frac{\sum_{i=1}^n (x_i - \bar{x})(y_i - \bar{y})}{\sqrt{\sum_{i=1}^n (x_i - \bar{x})^2 \sum_{i=1}^n (y_i - \bar{y})^2}} \quad (1)$$

where r denotes the PCC, y_i represents precipitation due to an SDHR event, and x_i is the TBB value. The absolute value of r is between 0 and 1. A negative value of r indicates that precipitation decreases with increasing TBB.

We also employed an ordinary least squares linear regression function to estimate SDHR precipitation:

$$y_i = a + bx_i \quad (2)$$

$$b = \frac{n \times \sum_{i=1}^n x_i y_i - \sum_{i=1}^n x_i \sum_{i=1}^n y_i}{n \times \sum_{i=1}^n x_i^2 - (\sum_{i=1}^n x_i)^2} \quad (3)$$

$$a = \bar{y} - b\bar{x} \quad (4)$$

where y_i is the precipitation due to an SDHR event, x_i is the TBB value, n is the number of samples, \bar{x} is the average SDHR precipitation value, \bar{y} is the average TBB value, and a and b are the fitting intercept and slope, respectively.

3. Spatiotemporal Distribution Characteristics of SDHR

Figure 2 shows the spatiotemporal distribution of SDHR along the CCR. The plot shown in Figure 2a shows that the frequency of SDHR decreases with increasing rainfall intensity, and the cumulative frequency value for the 20–30 mm precipitation intensity grade was significantly higher than that of other grades (206 occurrences, accounting for 62.2% of the total). SDHR with a precipitation intensity of ≥ 50 mm occurred least frequently (17 occurrences, accounting for only 5.1% of the total). SDHR events were recorded along the CCR from April to October (Figure 2b), most of which occurred between June and August. The month with the most SDHR events was July (115 occurrences, accounting for 34.7% of the total), followed by August (91 occurrences, accounting for 27.5%). October had the fewest, with only one event recorded. SDHR also exhibited evident diurnal variation characteristics along the CCR (Figure 2c). It occurred most frequently at night (260 occurrences, accounting for 78.5% of the whole-day total). The cumulative frequency for daytime events was low (71 occurrences, accounting for only 21.5% of the whole-day total). The times at which SDHR events most frequently occurred were 22:00–05:00 (all times given here are local time) and 06:00–09:00, with a peak at 01:00 (42 occurrences, accounting for 12.7% of the whole-day total), followed by 03:00 (36 occurrences, accounting for 10.9%). SDHR exhibited clear regional differences along the CCR; the spatial distribution can be described as “more SDHR in the middle section and less in the beginning and end sections” (Figure 2d). SDHR occurred most frequently in the Neijiang section of the line, and the highest number of occurrences (20 occurrences) was recorded in the Longchang Contry, Neijiang City (Figure 2d).

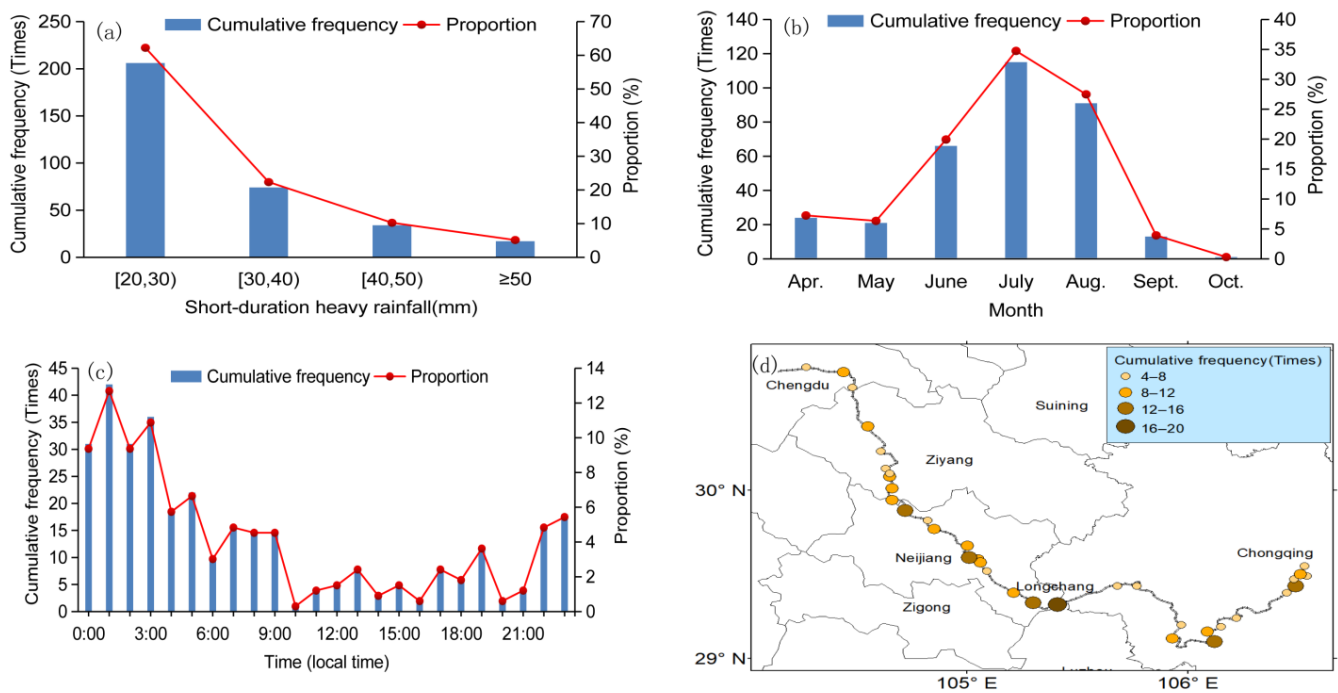


Figure 2. Characteristics of short-duration heavy rainfall events along the Chengdu–Chongqing Railway in 2019–2020. (a–c) Cumulative frequency plots which also show the proportion of the total number of occurrences represented by each category for (a) precipitation data, (b) monthly variation, and (c) diurnal variation. (d) Map showing the spatial distribution of SDHR events for the meteorological stations included in this study.

4. Relationship between SDHR and TBB and Its Estimating Equation

4.1. TBB Characteristics of SDHR

According to the observational characteristics of the FY-4A satellite, we recorded the TBB value closest to each meteorological station every 15 min and analyzed the variation in TBB for the periods 1 h before, during, and after the occurrence of SDHR. Figure 3 shows the change in average TBB with time for SDHR events that lasted for 1 h and for those that continued for 2 h consecutively. The x -axis represents time, where 0 min corresponds to the moment of onset of the SDHR. The plot shows that for SDHR events that lasted for only 1 h, TBB began to decline rapidly 1 h before the onset of the SDHR. At the onset, the TBB dropped to a low level of 221 K. During the SDHR event, TBB decreased further, reaching a minimum value of 214.2 K at 60 min. TBB then began to increase gradually, marking the end of the SDHR event. For SDHR events that lasted for 2 h consecutively, TBB also dropped rapidly during the 1 h period before the SDHR began. At the beginning of the SDHR event, TBB dropped to 222.2 K. As the SDHR continued, TBB also continued to decrease, approaching its minimum value after 60 min. However, as SDHR continued into a second hour, TBB continued to decrease slightly, reaching a minimum value of 207.6 K at 90 min. After this time, the TBB gradually increased, and the SDHR event ended. Thus, the plot shows that the SDHR events occur as TBB decreases to a minimum value, after which TBB rises, and the SDHR ceases. For longer SDHR events, TBB approaches its minimum value after 1 h but continues to decrease slightly—this could be used as an important indicator of whether SDHR is likely to continue.

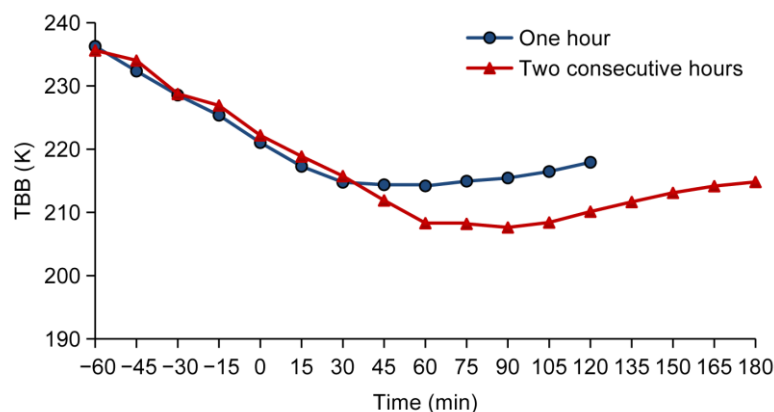


Figure 3. Changes in the average equivalent blackbody temperature (TBB) of short-duration heavy rainfall (SDHR) along the Chengdu–Chongqing Railway with time, during the period 2019–2020. (Note: On the x -axis, 0 indicates the moment of onset of SDHR, and negative values indicate the time before the onset of SDHR).

4.2. TBB Characteristics of the Different Levels of SDHR

The plots shown in Figure 4 illustrate the cumulative frequency with which TBB and minimum TBB observations were recorded during SDHR events along the CCR. The data are grouped into intervals, and the proportion of the total frequency accounted for by each interval is shown. As Figure 4a shows, during SDHR, the majority of the TBB values were recorded in the range 190–230 K, and values between 190 and 200 K were most frequently recorded (393 times, accounting for 23.7% of the total), followed by the 200–210 K range (346 times, accounting for 20.9%). Figure 4b shows the minimum TBB values recorded during SDHR events. The majority of the minimum TBB values were recorded in the range 180–230 K; within this range, values of 190–200 K were most frequently recorded (91 times, accounting for 27.5% of the total) followed by 200–210 K (74 times, accounting for 22.4%).

The TBB interval distribution of SDHR events was analyzed using four hourly rainfall categories: 20–30 mm, 30–40 mm, 40–50 mm, and ≥ 50 mm (Figure 4c,d). For SDHR events with an hourly rainfall of 20–30 mm, the majority of the TBB values were recorded in the range 190–230 K. Within this range, TBB values between 190 and 200 K were most frequently recorded, accounting for 19.9% of the total, followed by 200–210 K, accounting for 18.9%. The TBB distribution was similar for SDHR events with hourly precipitations of 30–40 mm and 40–50 mm: the majority of TBB values were recorded in the range 180–220 K, and, within this range, values between 190 and 200 K were most frequently recorded, accounting for 30% (for the 30–40 mm category) and 32.4% (for the 40–50 mm category) of the total, respectively. Both of these were significantly higher than the value for the 20–30 mm category. For SDHR events with hourly precipitation values of 30–40 mm and 40–50 mm, the 200–210 K interval accounted for 28.9% and 21.2% of the total, respectively. For SDHR events with rainfall values ≥ 50 mm, the majority of the TBB values were recorded in the ranges 180–210 K and 220–230 K; TBB values in the 190–200 K interval were most frequently recorded, accounting for 27.1% of the total, followed by 220–230 K, accounting for 22.4%. The figure also shows that the proportion of TBB values belonging to the lowest interval 180–190 K increases as the SDHR events increase in magnitude (i.e., higher rainfall intensity values). The interval distribution for minimum TBB values was similar to that for TBB (Figure 4e,f), but the proportion of minimum TBB values belonging to the 180–190 K interval for each SDHR rainfall grade was significantly higher than for TBB.

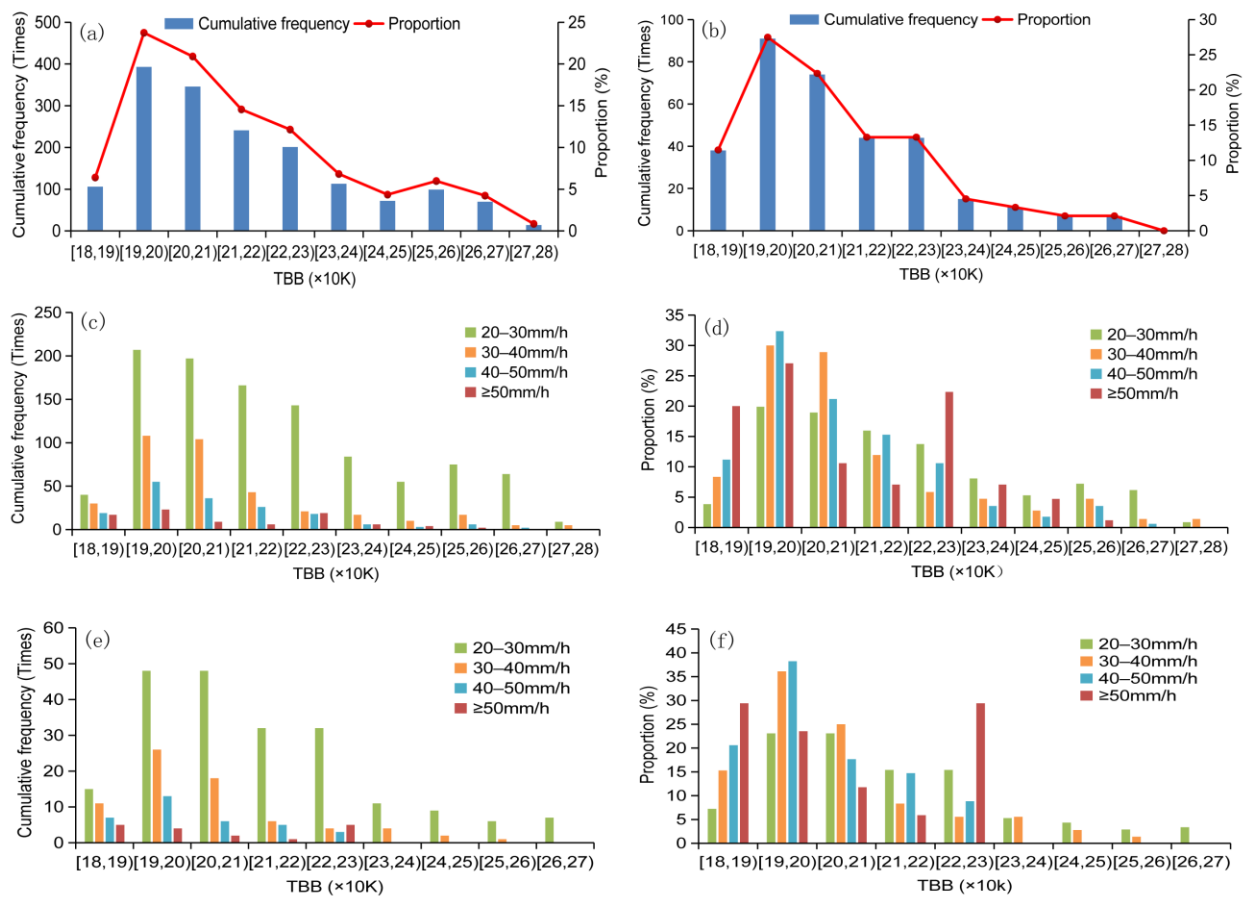


Figure 4. Cumulative frequency values for equivalent blackbody temperature (TBB) observations, and the proportion of the total accounted for by each interval, for short-duration heavy rainfall (SDHR) events along the Chengdu–Chongqing Railway. (a) Frequency and proportion for intervals of TBB; (b) frequency and proportion for intervals of minimum TBB; (c,d) TBB frequency (c) and proportion (d) with rainfall intensity categories; (e,f) minimum TBB frequency (e) and proportion (f) with rainfall intensity categories.

The above analysis indicates that the majority of TBB values were recorded in the range 190–230 K during SDHR events, and values between 190 and 200 K were most frequently recorded within this range. For SDHR events with rainfall values of 20–30 mm, the majority of TBB values were recorded in the range 190–230 K, and values between 190 and 200 K were most frequently recorded within this range. For SDHR events with rainfall values of 30–40 mm and 40–50 mm, the majority of the TBB values were recorded in the range 180–220 K, most of which were between 190 and 200 K. Finally, for SDHR events with rainfall values ≥ 50 mm, the majority of the TBB values were recorded in the ranges 180–210 K and 220–230 K, with the 190–200 K interval accounting for the largest proportion of these values.

4.3. Relationship between SDHR and TBB and Its Estimating Equation

To further analyze the relationship between SDHR and TBB, correlation coefficients were calculated between hourly precipitation and mean TBB, and between hourly precipitation and minimum TBB, for three periods: 1 h before the onset of SDHR, during the occurrence of SDHR, and one hour after the cessation of SDHR (Table 1). As can be seen from the table, hourly precipitation had the most significant relationship with minimum TBB at the time of SDHR occurrence, showing a significant negative correlation with a correlation coefficient of -0.2638 . This indicated that a lower TBB value during the occurrence of SDHR was associated with higher rainfall intensity.

Table 1. Correlation coefficients between hourly precipitation and equivalent black body temperature (TBB) during short-duration heavy rainfall (SDHR) events.

	One Hour before SDHR	During the Occurrence of SDHR	One Hour after SDHR
Mean TBB	−0.1025	−0.2469	−0.2422
Minimum TBB	−0.1358	−0.2638	−0.2244

(Note: A correlation coefficient ≥ 0.188 indicates a statistically significant relationship at the 99% confidence level).

Through the above analysis, we have established that SDHR is likely to occur when TBB falls within the range 190–230 K. In order to further judge the precipitation of SDHR, linear regression was used to obtain a best-fit line for the precipitation and minimum TBB data, yielding the following rainfall estimation equation for SDHR events along the CCR:

$$y = 59.5952 - 0.1421x \tag{5}$$

where y is the hourly precipitation for an SDHR event, and x is the minimum TBB. The equation passes the significance test at a 99% confidence level.

From 02:00 to 07:00 on 18 August 2021, a large-scale SDHR weather process was observed along the CCR. This process was used in this study to test the rainfall estimation equation for SDHR. Table 2 shows the estimated and observed values for this event. The absolute error between the predicted rainfall and the measured rainfall was generally less than 10 mm, the average absolute error was 8.2 mm, the absolute error rate was generally less than 30%, and the average absolute error rate was 25.6%. These values show that the estimated rainfall for the SDHR was consistent with the actual measured rainfall values, confirming that the equation can be used to produce reasonable rainfall estimates for SDHR events along the CCR.

Table 2. Measured rainfall, estimated rainfall, and results of statistical testing for short-duration heavy rainfall for the period 02:00–07:00 on 18 August 2021.

Local Time	Site	2:00		3:00			4:00			5:00		6:00		7:00
		SHV	LC	ZZ	YX	FX	YLB	LGM	YLB	SFT	ZX	WF	RH	SBT
Measured rainfall (mm)		41.5	40.8	38.7	35	48.8	34.4	25.3	41	21.4	20.6	32.3	34.1	26.7
Estimated rainfall (mm)	Equation (5)	31.2	30.6	30.3	31.1	30.4	29.7	32.9	31.5	32.2	32.6	29.3	29.6	30.6
	Equation (6)	32.2	31.4	31.0	32.0	31.1	30.4	34.6	32.6	33.6	34.3	29.9	30.3	31.5
Absolute error (mm)	Equation (5)	10.3	10.2	8.4	3.9	18.4	4.7	7.6	9.5	10.8	12	3	4.5	3.9
	Equation (6)	9.3	9.4	7.7	3.0	17.7	4.0	9.3	8.4	12.2	13.7	2.4	3.8	4.8
Absolute error rate (%)	Equation (5)	24.8	25.0	21.7	11.1	37.7	13.7	30.0	23.2	50.5	58.3	9.3	13.2	14.6
	Equation (6)	22.4	23.0	19.9	8.6	36.3	11.6	36.8	20.5	57.0	66.5	7.4	11.1	18.0

(Note: SHV: Sanhe Village; LC: Longchang; ZZ: Zizhong; YX: Yingxiang; FX: Fuxi; YLB: Yangliu Beach; LGM: Lugao Mountain; SFT: Shuangfeng Temple; ZX: Zixi; WF: Wufeng; RH: Renhe; SBT: Shibantan).

Polynomial regression was also used to calculate a best-fit line, and the following polynomial regression estimation equation for SDHR rainfall along the CCR was obtained:

$$y = 0.016x^2 - 0.8281x + 133.7712 \tag{6}$$

where y is the hourly precipitation of an SDHR event, and x is the minimum TBB. This equation also passes the significance test at a 99% confidence level. By comparing estimating Equations (5) and (6), it was found that the absolute error and absolute error rate of the estimates produced using Equation (6) were slightly lower than those of Equation (5) (Table 2) in most cases, but, in general, there was little difference between them. The mean absolute error for Equation (5) was 8.2 mm; for Equation (6), it was slightly lower, at

8.1 mm. For Equation (5), the mean absolute error rate was 25.6%, while the mean absolute error rate for Equation (6) was slightly higher, at 26.1%. These results demonstrate that an estimating equation for hourly rainfall values during SDHR along the CCR could be obtained using linear regression—estimating Equation (5) was able to provide reasonably accurate estimates.

It can also be seen from Table 2 that the variation in the measured rainfall was larger than that of the estimated rainfall from Equations (5) and (6), and, sometimes, the absolute error between the real time rainfall and the estimate rainfall was more than 10 mm, which indicated that the estimation equations had some shortcomings in the estimation of the intensity of SDHR. However, the estimated rainfall from Equations (5) and (6) were all above 20 mm, which were good estimates of this SDHR event. The estimation equations can help improve the forecast and warning of SDHR along the CCR.

5. Conclusions

In this study, the spatiotemporal distribution characteristics of SDHR along the CCR and its relationship with TBB have been revealed using high-resolution data from the FY-4A satellite and hourly precipitation data from meteorological stations, for the period 2019–2020. The results are as follows:

- (1) The frequency of SDHR along the CCR decreased with increasing rainfall intensity. SDHR events with an hourly rainfall of 20–30 mm occurred most frequently, and those with hourly rainfall ≥ 50 mm occurred least frequently. SDHR events were mainly concentrated in June to August and occurred most frequently in July. SDHR showed clear diurnal variation, occurring most frequently at night, particularly between 22:00–05:00 and 06:00–09:00, with a peak at 01:00.
- (2) TBB decreased rapidly 1 h before the occurrence of SDHR along the CCR. SDHR was accompanied by a decrease in TBB to its minimum value, after which TBB increased, and the SDHR ceased. In cases where TBB approached a minimum value at 1 h but continued to drop slightly, SDHR continued.
- (3) During SDHR events, the majority of the TBB values were recorded in the range 190–230 K; within this range, values between 190 and 200 K were most frequently recorded. For SDHR events with an hourly rainfall of 20–30 mm, the majority of the TBB values were recorded in the range 190–230 K; for rainfall values of 30–40 mm and 40–50 mm, the majority of the TBB values were recorded in the range 180–220 K; and for rainfall values ≥ 50 mm, the majority of the TBB values were recorded in the ranges 180–210 K and 220–230 K. In general, lower TBB values are associated with more intense SDHR. An estimating equation was established for the rainfall values of SDHR events. The estimates were found to be consistent with the actual rainfall measurements, which could enable future estimates of rainfall values for SDHR along the CCR.

The quantification of the relationship between SDHR and TBB along the CCR provided here could be of practical value in forecasting and providing early warnings of SDHR. However, due to inaccuracies in the classification of hourly SDHR observations, some of the findings presented here may require further refinement using more detailed data. In addition, it is important to note that this study only analyzes data from a specific time period and location; thus, the results may not be generalizable to other regions or time periods.

Author Contributions: Conceptualization, X.L. and Y.C.; methodology, X.L. and J.G.; software, X.L., W.S. and J.D.; formal analysis, X.L. and Y.C.; investigation, X.L., Y.C. and J.G.; resources, X.L., J.G. and W.S.; data curation, X.L. and J.D.; writing—original draft preparation, X.L.; writing—review and editing, X.L. and Y.C.; visualization, X.L.; supervision, Y.C. and J.G.; project administration, W.S. and J.D.; funding acquisition, X.L. and Y.C.. All authors have read and agreed to the published version of the manuscript.

Funding: This study was supported by the Sichuan Science and Technology Program (Grant/Award Numbers: 2022YFS0543, 2021YFS0326); the Innovation Team of the Southwest Regional Meteorological Center of China Meteorological Administration (Grant No. XNQYCXTD202203, Grant No. XNQYCXTD202201); and the 2021 Science and Technology Development Fund of Heavy Rain and Drought-Flood Disasters in Plateau and Basin Key Laboratory of Sichuan Province (Grant No. SC-QXKJYJXMS202118).

Institutional Review Board Statement: Not applicable.

Informed Consent Statement: Not applicable.

Data Availability Statement: The data used in this study and their availability are as follows: (1) Land surface precipitation data are from the observational systems of the China Meteorological Administration. The datasets generated and/or analyzed during the current study are available from the corresponding author upon reasonable request. (2) TBB data are from the FY4A geostationary weather satellite provided by the National Satellite Meteorological Center, China Meteorological Administration (<http://www.nsmc.org.cn/nsmc/en/home/index.html> (accessed on 10 April 2023)).

Conflicts of Interest: The authors declare no conflict of interest.

References

1. Chen, J.; Zheng, Y.G.; Zhang, X.L.; Zhu, P.J. Distribution and diurnal variation of warm-season short-duration heavy rainfall in relation to the MCSs in China. *Acta Meteor. Sin.* **2013**, *27*, 868–888. [[CrossRef](#)]
2. Kendon, E.J.; Blenkinsop, S.; Fowler, H.J. When will we detect changes in short-duration precipitation extremes? *J. Clim.* **2018**, *31*, 2945–2964. [[CrossRef](#)]
3. Liu, K.; Wang, M.; Zhou, T.J. Increasing costs to Chinese railway infrastructure by extreme precipitation in a warmer world. *Transpor. Res. D-Transp. Environ.* **2021**, *93*, 102797. [[CrossRef](#)]
4. Palin, E.J.; Oslakovic, I.S.; Gavin, K.; Quinn, A. Implications of climate change for railway infrastructure. *WIREs Clim. Chang.* **2021**, *12*, e728. [[CrossRef](#)]
5. Ma, J.L.; Yao, X.P. Summer extreme precipitation in the key region of the Sichuan-Tibet Railway. *Adv. Atmos. Sci.* **2023**, *40*, 843–855. [[CrossRef](#)]
6. Alexander, L.V.; Zhang, X.; Peterson, T.C.; Caesar, J.; Gleason, B.; Klein Tank, A.M.G.; Haylock, M.; Collins, D.; Trewin, B.; Rahimzadeh, F.; et al. Global observed changes in daily climate extremes of temperature and precipitation. *J. Geophys. Res.-Atmos.* **2006**, *111*, D05109. [[CrossRef](#)]
7. Wang, Y.Q.; Zhou, L. Observed trends in extreme precipitation events in China during 1961–2001 and the associated changes in large-scale circulation. *Geophys. Res. Lett.* **2005**, *32*, L09707. [[CrossRef](#)]
8. Zhai, P.M.; Zhang, X.B.; Wan, H.; Pan, X.H. Trends in total precipitation and frequency of daily precipitation extremes over China. *J. Clim.* **2005**, *18*, 1096–1108. [[CrossRef](#)]
9. Westra, S.; Fowler, H.; Evants, J.P.; Alexander, L.V.; Berg, P.; Johnson, F.; Kendon, E.J.; Lenderink, G.; Roberts, N.M. Future changes to the intensity and frequency of short-duration extreme rainfall. *Rev. Geophys.* **2014**, *52*, 522–555. [[CrossRef](#)]
10. Donat, M.G.; Lowry, A.L.; Alexander, L.V.; O’Gorman, P.A.; Maher, N. More extreme precipitation in the world’s dry and wet regions. *Nat. Clim. Chang.* **2016**, *6*, 508–513. [[CrossRef](#)]
11. Myhre, G.; Alterskjar, K.; Stjern, C.W.; Hodnebrog, Q.; Marelle, L.; Samset, B.H.; Sillmann, J.; Schaller, N.; Fischer, E.; Schulz, M.; et al. Frequency of extreme precipitation increases extensively with event rareness under global warming. *Sci. Rep.* **2019**, *9*, 16063. [[CrossRef](#)]
12. Martel, J.L.; Mailhot, A.; Brissette, F. Global and regional projected changes in 100-yr subdaily, daily, and multiday precipitation extremes estimated from three large ensembles of climate simulations. *J. Clim.* **2020**, *33*, 1089–1103. [[CrossRef](#)]
13. Hichens, N.M.; Brooks, H.E.; Schumacher, R.S. Spatial and temporal characteristics of heavy hourly rainfall in the United States. *Mon. Weather Rev.* **2013**, *141*, 4564–4575. [[CrossRef](#)]
14. Li, Z.; Yang, D.W.; Hong, Y.; Zhang, J.; Qi, Y.C. Characterizing spatiotemporal variations of hourly rainfall by gauge and radar in the mountainous three gorges region. *J. Appl. Meteorol. Clim.* **2014**, *53*, 873–889. [[CrossRef](#)]
15. Li, H.Q.; Cui, X.P.; Zhang, D.L. A statistical analysis of hourly heavy rainfall events over the Beijing metropolitan region during the warm seasons of 2007–2014. *Int. J. Climatol.* **2017**, *37*, 4027–4042. [[CrossRef](#)]
16. Jiang, X.L.; Luo, Y.L.; Zhang, D.L.; Wu, M.W. Urbanization enhanced summertime extreme hourly precipitation over the Yangtze river delta. *J. Clim.* **2020**, *33*, 5809–5826. [[CrossRef](#)]
17. Li, J.; Yu, R.C.; Sun, W. Duration and seasonality of hourly extreme rainfall in the central eastern China. *Acta Meteor. Sin.* **2013**, *27*, 799–807. [[CrossRef](#)]
18. Zhang, H.; Zhai, P.M. Temporal and spatial characteristics of extreme hourly precipitation over eastern China in the warm season. *Adv. Atmos. Sci.* **2011**, *28*, 1177–1183. [[CrossRef](#)]
19. Zheng, Y.G.; Gong, Y.D.; Chen, J.; Tian, F.Y. Warm-season diurnal variations of total, stratiform, convective, and extreme hourly precipitation over central and eastern China. *Adv. Atmos. Sci.* **2019**, *36*, 143–159. [[CrossRef](#)]

20. Luo, Y.L.; Wu, M.W.; Ren, F.M.; Li, J.; Wong, W.K. Synoptic situations of extreme hourly precipitation over China. *J. Clim.* **2016**, *29*, 8703–8719. [[CrossRef](#)]
21. Wu, M.; Wu, C.C.; Yen, T.H.; Luo, Y.L. Synoptic analysis of extreme hourly precipitation in Taiwan during 2003–12. *Mon. Weather Rev.* **2017**, *145*, 5123–5140. [[CrossRef](#)]
22. Yang, P.; Ren, G.Y.; Hou, W.; Liu, W.D. Spatial and diurnal characteristics of summer rainfall over Beijing municipality based on a high-density AWS dataset. *Int. J. Climatol.* **2013**, *33*, 2769–2780. [[CrossRef](#)]
23. Liang, P.; Ding, Y. The long-term variation of extreme heavy precipitation and its link to urbanization effects in Shanghai during 1916–2014. *Adv. Atmos. Sci.* **2017**, *34*, 321–334. [[CrossRef](#)]
24. Wang, D.S.; Wang, X.W.; Liu, L.; Wang, D.G.; Zeng, Z.Z. Urban signatures in the spatial clustering of precipitation extremes over mainland China. *J. Hydrometeorol.* **2021**, *22*, 639–656. [[CrossRef](#)]
25. Yang, P.; Ren, G.Y.; Yan, P.C. Evidence for a strong association of short-duration intense rainfall with urbanization in the Beijing urban area. *J. Clim.* **2017**, *30*, 5851–5870. [[CrossRef](#)]
26. Wu, M.W.; Luo, Y.L.; Chen, F.; Wong, W.K. Observed link of extreme hourly precipitation changes to urbanization over coastal south China. *J. Appl. Meteor. Climatol.* **2019**, *58*, 1799–1819. [[CrossRef](#)]
27. Tian, F.Y.; Zheng, Y.G.; Zhang, T.; Zhang, X.L.; Mao, D.Y.; Sun, J.H.; Zhao, S.X. Statistical characteristics of environmental parameters for warm season short-duration heavy rainfall over central and eastern China. *J. Meteor. Res.* **2015**, *29*, 370–384. [[CrossRef](#)]
28. Meng, Y.N.; Sun, J.H.; Zhang, Y.C.; Fu, S.M. A 10-Year climatology of mesoscale convective systems and their synoptic circulations in the southwest mountain area of China. *J. Hydrometeorol.* **2020**, *22*, 23–41. [[CrossRef](#)]
29. Ma, R.Y.; Sun, J.H.; Yang, X.L. A 7-Yr climatology of the initiation, decay, and morphology of severe convective storms during the warm season over north China. *Mon. Weather Rev.* **2021**, *149*, 2599–2612. [[CrossRef](#)]
30. Zou, Q.L.; Cui, X.P.; Hao, S.F. The statistical relationship of lightning activity and short-duration rainfall events over Guangzhou, China, in 2017. *Weather Forecast.* **2022**, *37*, 601–615. [[CrossRef](#)]
31. Chen, Y.R.; Li, Y.Q. A thermodynamic condition affecting the movement of a southwest China vortex case. *Meteorol. Atmos. Phys.* **2022**, *134*, 36. [[CrossRef](#)]
32. Chen, Y.R.; Li, Y.Q.; Kang, L. An index reflecting mesoscale vortex–vortex interaction and its diagnostic applications for rainstorm area. *Atmos. Sci. Lett.* **2019**, *20*, e902. [[CrossRef](#)]
33. Chen, Y.R.; Li, Y.Q. Analysis of a late-autumn rainstorm in the Sichuan basin on the eastern side of the Tibetan plateau. *Adv. Meteorol.* **2019**, *2019*, 8797368. [[CrossRef](#)]
34. Chen, Y.R.; Li, Y.Q.; Qi, D.M. Analysis of the convective characteristics during the mutual evolution of an inverted trough/low vortex and its induced rainstorm over the northeastern Sichuan basin, China. *Meteorol. Atmos. Phys.* **2019**, *131*, 807–825. [[CrossRef](#)]
35. Chen, Y.R.; Li, Y.Q. Convective Characteristics and formation conditions in an extreme rainstorm on the eastern edge of the Tibetan plateau. *Atmosphere* **2021**, *12*, 381. [[CrossRef](#)]
36. Chen, Y.R.; Li, Y.Q.; Liu, X.C.; Zhu, L. Helicity characteristics of cyclonic vortices and their effect on convection in a wide-ranging extreme rainstorm in China. *Atmos. Sci. Lett.* **2023**, *24*, e1162. [[CrossRef](#)]
37. Deng, M.Y.; Lu, R.Y.; Li, C.F. Contrasts between the interannual variations of extreme rainfall over western and eastern Sichuan in mid-summer. *Adv. Atmos. Sci.* **2022**, *39*, 999–1011. [[CrossRef](#)]
38. Zheng, Y.G.; Xue, M.; Li, B.; Chen, J.; Tao, Z.Y. Spatial characteristics of extreme rainfall over China with hourly through 24-hour accumulation periods based on national-level hourly rain gauge data. *Adv. Atmos. Sci.* **2016**, *33*, 1218–1232. [[CrossRef](#)]
39. Huang, J.; Sun, S.L.; Xue, Y.; Li, J.J.; Zhang, J.C. Spatial and temporal variability of precipitation and dryness/wetness during 1961–2008 in Sichuan province, west China. *Water Resour. Manag.* **2014**, *28*, 1655–1670. [[CrossRef](#)]
40. Li, J.; Zhao, Y.D.; Iqbal, J. Variation patterns of extreme precipitation and relation to ocean-atmospheric climate in Sichuan province China from 1961 to 2017. *Theor. Appl. Climatol.* **2019**, *137*, 3009–3026. [[CrossRef](#)]
41. Yang, J.; Zhang, Z.Q.; Wei, C.Y.; Lu, F.; Guo, Q. Introducing the new generation of Chinese geostationary weather satellites, Fengyun-4. *Bull. Am. Meteor. Soc.* **2017**, *98*, 1637–1658. [[CrossRef](#)]
42. Yu, Z.F.; Ma, S.; Han, D.; Li, G.L.; Yan, W.; Liu, J.D. Physical and optical properties of clouds in the southwest Vortex from FY-4A cloud retrievals. *J. Appl. Meteor. Climatol.* **2022**, *61*, 1123–1138. [[CrossRef](#)]
43. Xu, L.; Cheng, W.; Deng, Z.R.; Liu, J.J.; Wang, B.; Lu, B.; Wang, S.D.; Dong, L. Assimilation of the FY-4A AGRI clear-sky radiance data in a regional numerical model and its impact on the forecast of the “21·7” Henan extremely persistent heavy rainfall. *Adv. Atmos. Sci.* **2022**, *40*, 920–936. [[CrossRef](#)]
44. Shao, J.L.; Gao, H.; Wang, X.; Zhang, Q.Q. Application of Fengyun-4 satellite to flood disaster monitoring through a rapid multi-temporal synthesis approach. *J. Meteor. Res.* **2020**, *34*, 720–731. [[CrossRef](#)]
45. Pearson, K. VII. Mathematical contributions to the theory of evolution. -III. Regression, heredity, and panmixia. *Philos. Trans. R. Soc. Lond.* **1896**, *187A*, 253–318. [[CrossRef](#)]

Disclaimer/Publisher’s Note: The statements, opinions and data contained in all publications are solely those of the individual author(s) and contributor(s) and not of MDPI and/or the editor(s). MDPI and/or the editor(s) disclaim responsibility for any injury to people or property resulting from any ideas, methods, instructions or products referred to in the content.